Large-scale flow of Indian Ocean asthenosphere driven by Réunion plume

G. Barruol [1,2]*, K. Sigloch [3], J.-R. Scholz [1,2], A. Mazzullo[1], E. Stutzmann[1], J.-P. Montagner [1], S. Kiselev[4], F. R. Fontaine [1,2], L. Michon[1,2], C. Deplus[1] and J. Dyment [1]

Volcanic hotspot islands are thought to be surface manifestations of mantle plumes that rise from the core–mantle boundary. When mantle plumes approach the surface, their mostly vertical rise must be deflected into near-horizontal flow beneath tectonic plates. This creates an opportunity to constrain their dynamics and their interactions with lithospheric plates and mid-ocean ridges. Seafloor observations have been used to propose that a focused flow in the asthenosphere transports plume heat to the nearest mid-ocean ridge, where it efficiently dissipates through formation of lithosphere. Here we present imaging results from a seismological survey of a proposed plume-to-ridge flow channel between the Réunion hotspot and the Central Indian Ridge. Rayleigh-wave tomography and shear-wave splitting confirm the presence of a channelized flow of shallow asthenosphere, eastward from the hotspot to the spreading ridge. At a larger scale, a deeper reservoir of hot asthenosphere fills vast tracts of the Indian Ocean basin east and north of Réunion Island. Its flows, decoupled from overlying lithospheres, are also directed towards the Central Indian Ridge but extend well beyond, tapped but not significantly depleted by the spreading ridge. Based on seismic and geochemical observations, we suggest that this hidden heat reservoir is generated and driven by the mantle plume, which buffers more heat near the surface than expected.

Since Morgan's proposal of the deep convection plume hypothesis[1], Réunion has been a prime candidate for expressing such a deeply rooted 'primary' mantle upwelling[1,2]. The island (Fig. 1) is among the most active volcanoes globally, and features a hotspot-type, enriched geochemistry. It is located >1,000 km from the closest plate boundary at the young end of a 5,500 km long, time-progressive volcanic track that emerged from the Deccan flood basalts of India ~65 million years ago (Ma)[1,3,4]. The lowermost mantle under the region is anomalously slow in global tomography models[5–7], consistent with upwelling from the core–mantle boundary, but a surface connection has remained debatable due to insufficient seismic imaging resolution in the mid and upper mantle, as for other oceanic hotspots. Morgan complemented his deep plume hypothesis by the prediction that upwelling plumes, acting as a heat source near the surface, may establish a vigorous connection to nearby spreading ridges (heat sinks) via pipeline-like flow in the asthenosphere[8]. Citing the Réunion, Galapagos and Kerguelen systems as examples, he postulated such a plume–ridge interaction for all the hotspots that had spawned and initially captured a spreading ridge, which subsequently 'escaped' to a moderate distance. Réunion's pipeline would have developed when the Central Indian Ridge (CIR) gradually moved away and east of Réunion after 34 Ma (refs. [8–10]). Surface evidence supporting plume–ridge interaction includes:

1. Rodrigues Ridge (Fig. 1a)—an aseismic, east–west striking bathymetric high that projects the connection over time between Réunion's hotspot track and the CIR—presumably formed through a volcanic upward leakage of the channel flow, from at least 7–10 Ma (ref. [4]) to 1.5 Ma (ref. [11]).
2. Hotspot signature in the nearest CIR segment between Marie Celeste and the Egeria fault zones (~17–21° S). The segment protrudes westward, is exceptionally long, unusually elevated and asymmetric, with a smoother bathymetry on its western ridge flank (Fig. 1a), which all suggest a preferential, hot feeding from Réunion.
3. Réunion hotspot signature[12–15] in the major and trace elements and isotopic compositions of basalts dredged on the CIR between 18 and 21° S, and on the easternmost Rodrigues Ridge (Gasitao and Three Magi Ridges).
4. Slow earthquakes on the Marie Celeste transform fault, which could indicate the presence of lubricating, hotspot-generated melts[16].

Seismological imaging of lithosphere and asthenosphere

The RHUM-RUM experiment[17] (Réunion Hotspot and Upper Mantle—Réunions Unterer Mantel, http://www.rhum-rum.net/) instrumented the area of Fig. 1a with 57 broadband ocean-bottom seismometers (OBS) for 13 months, and with 20 island stations for 2–4 years (details in Methods). The largest oceanic plume imaging effort to date in terms of area and instruments deployed simultaneously, RHUM-RUM also represents the first long-term deployment above one of Morgan's hypothesized asthenospheric flow channels[8].

To infer the patterns of heat and material flow in the upper 300 km, we combined the complementary methods of anisotropic surface-wave tomography (fundamental-mode Rayleigh waves, 30–300 s) (ref. [18]) and shear-wave splitting measurements[19]. Isotropic shear-velocity anomalies ($\delta V_s/V_s$) are a proxy primarily for mantle temperature. Azimuthal anisotropy of $\delta V_s/V_s$ is a proxy for the current or past mantle flow. Compared to the previously very sparse seismic instrumentation, RHUM-RUM substantially improved the seismic resolution across much of the Indian Ocean basin (Supplementary Fig. 1).
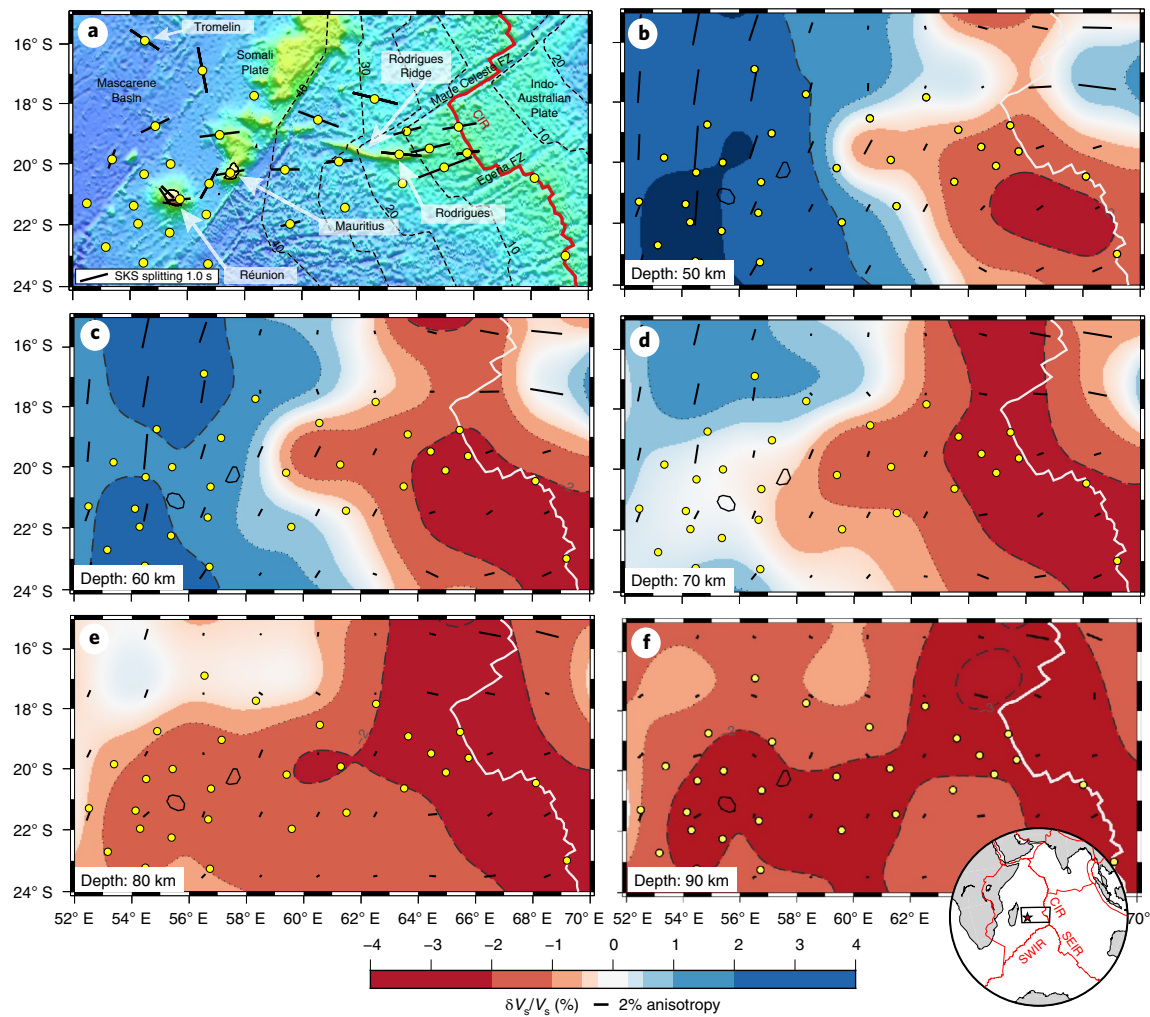
Fig. 1 | Seismological imaging of the Rodrigues Corridor region, from Réunion to the CIR. a, Bathymetric map showing SKS splitting measurements[19,26] (black bars) at RHUM-RUM ocean-bottom and island stations (yellow dots). Bar lengths and azimuths represent the magnitudes and fast directions of SKS splitting. Grey dashed lines are seafloor age isochrons up to 40 Ma. **b–f**, Shear-wave velocity variations $\delta V_s/V_s$ (red, slow; blue, fast) from Rayleigh-wave tomography[18] at depths of 50 (**b**), 60 (**c**), 70 (**d**), 80 (**e**) and 90 (**f**) km. Thick dashed and thin dotted lines are isocontours of $\delta V_s/V_s = \pm 2\%$ and $\pm 1\%$, respectively. Black bars are azimuthal anisotropy estimates from tomography. Anisotropy bars in all panels are normalized to the '2% anisotropy' bar shown beneath the colour bar. FZ, fracture zone; SWIR, Southwest Indian Ridge; SEIR, Southeast Indian Ridge.

Beneath the CIR, tomography[18] shows a band of slower-than-average $\delta V_s/V_s$ at 50–90 km depth (red in Fig. 1b–f), as expected from thin or absent lithosphere. Réunion and Mauritius are underlain by faster-than-average shear velocities down to about a 60 km depth (dark blue in Fig. 1b,c), consistent with 60–90 Myr old lithosphere in the Mascarene Basin[20].

Under the Rodrigues corridor, which stretches ~1,000 km from Réunion to the CIR, the asthenosphere reaches closer to the surface than to its north or south. From 50 to 90 km depths (Fig. 1b–f), this tongue of slow asthenosphere protrudes progressively westward from the anomalous CIR segment, deepening to 80–90 km under Réunion. The tongue's north–south width of ~400 km is resolved (Methods and Supplementary Figs. 2 and 3), and roughly matches the north–south extent of the anomalous CIR segment (~17–21° S (Fig. 1a)).

On the larger scale of the Indian Ocean basin, Fig. 2 presents the tomography model and Fig. 3a maps the lithospheric thickness, or depth of the lithosphere–asthenosphere boundary (LAB), estimated as the 1,200 °C isotherm derived from isotropic $\delta V_s/V_s$ (ref. [21]) (Methods and Supplementary Fig. 6). The lithosphere is observed to thicken perpendicularly away from the CIR, that is, with seafloor age, as expected for conductive half-space cooling. The east–west

'groove' of the thinned Rodrigues corridor lithosphere in Fig. 3a, with its gentler thickening gradient and shallowing asthenosphere (Fig. 2b,c), is unexpected and must reflect additional heat flux.

Apart from the Rodrigues corridor, slow $\delta V_s/V_s$ anomalies in the upper 100 km in Fig. 2b,c correlate strongly with the Indian Ocean's four spreading ridges (Carlsberg, Central, Southwest and Southeast Indian Ridges). This predictable pattern changes completely below 100 km, where slow $\delta V_s/V_s$ anomalies are no longer associated with the mid-ocean ridges (Fig. 2d–f). Instead, slow asthenosphere is abundant beneath the eastern half of the Somali Plate, stretching east and northeast of Madagascar and towards the CIR. Below 200 km, this vast slow anomaly is centred beneath the Mascarene Basin, where it bottoms out at or below 350 km, our deepest resolvable depth.

Discernible in some previous tomographies[22,23], this basin-sized body of slow asthenosphere has come into sharp focus through the dense RHUM-RUM data (Supplementary Fig. 1). We term it 'Mascarene Basin Asthenospheric Reservoir' (MBAR) and its connectivity across depths is highlighted in Fig. 3b, a three-dimensional (3D) rendering of slow anomalies located deeper than 100 km (which eliminates spreading ridges). The MBAR extends north and
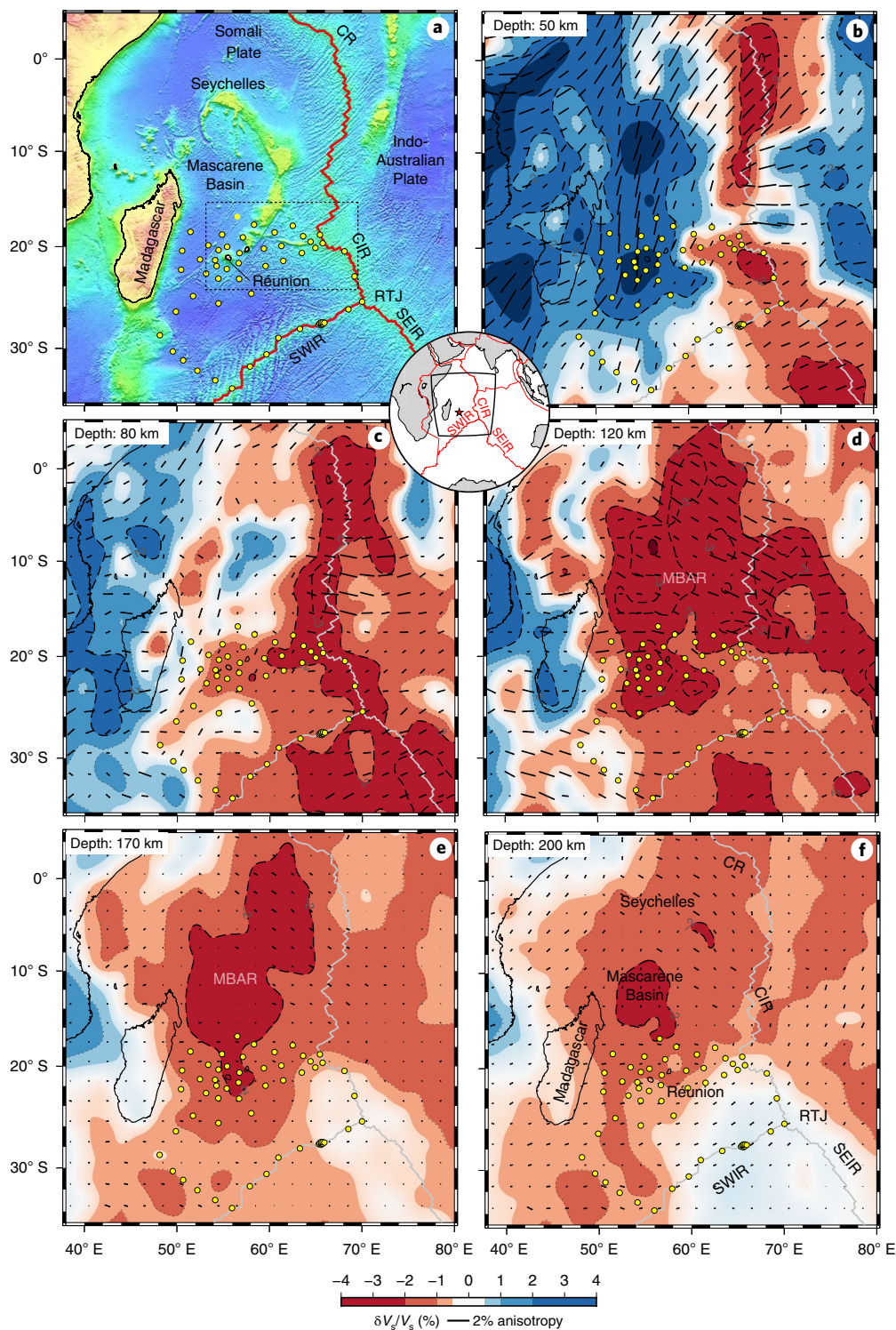
Fig. 2 | Surface-wave tomography[18] **of the western Indian Ocean. a**, Bathymetric map showing the RHUM-RUM OBS locations (yellow dots) and spreading ridges: SWIR, SEIR, CIR, Carlsberg Ridge (CR) and Rodrigues Triple Junction (RTJ). **b–f**, Shear-wave velocity variations $\delta V_s/V_s$ at depths of 50 (**b**), 80 (**c**), 120 (**d**), 170 (**e**) and 200 (**f**) km, shown on the same colour scale as that in Fig. 1. Black bars show the azimuthal anisotropy estimates from tomography, as in Fig. 1. The dashed square shows the area of Fig. 1.

east of Réunion, and its southern limit coincides with the Rodrigues corridor. At latitudes of about 6–17° S, MBAR spills beneath the CIR and across to the Indo-Australian Plate, but does not extend to the region's other spreading centres, that is, the Rodrigues Triple Junction, Southwest Indian Ridge and East African Rift System (Fig. 2d–f and Fig. 3b).

Asthenospheric flow inferred from seismic anisotropy

Seismic anisotropy is dominantly controlled by the alignment of olivine crystals' fast axis [100] in the flow direction[24,25] (details in Methods), and thus constitutes a proxy for upper-mantle flow.

Beneath the seismic stations, azimuthal anisotropy is robustly constrained by 88 SKS splitting measurements[19], which provide
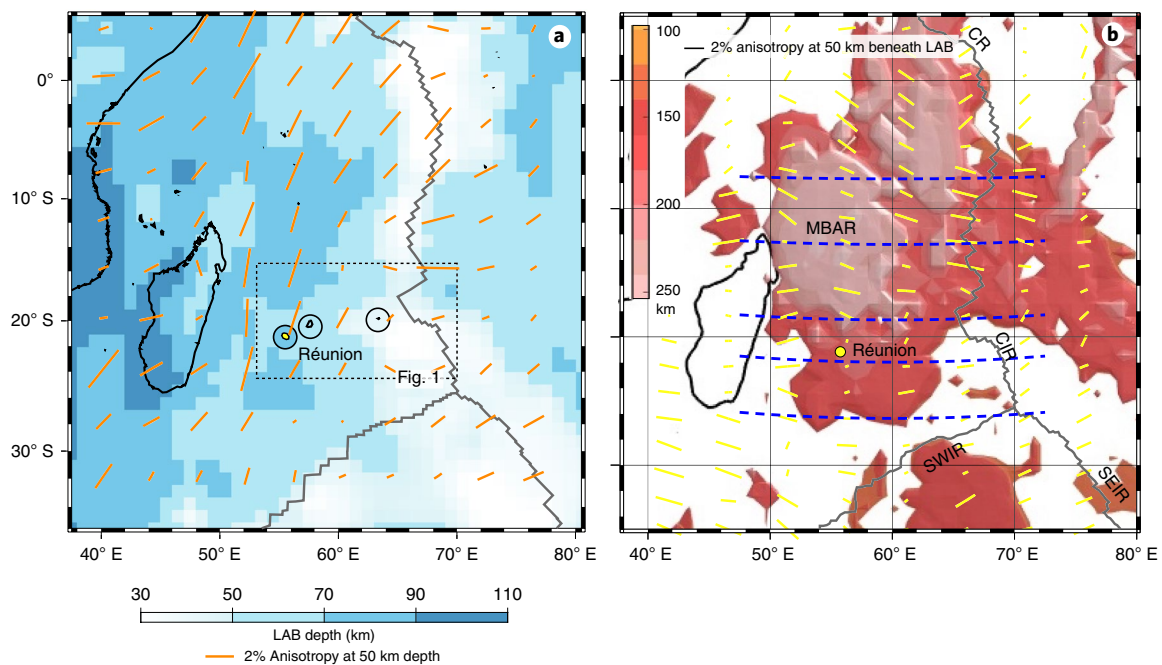
Fig. 3 | Shape and dynamics of the MBAR. a, Map of lithosphere thickness or LAB depth (blue shades), estimated from surface-wave tomography[21] as the depth of the 1,200 °C isotherm. Blue shades inside the black circles are independent LAB depth estimates under Réunion, Mauritius and Rodrigues islands from receiver function and surface-wave dispersion data[49]. Orange bars show the azimuthal anisotropy in the lithosphere at 50 km depth, normalized to the 2% anisotropy scale bar in the legend. **b**, 3D rendering of an anomalously slow asthenosphere ($-\delta V_s/V_s > 1.5\%$ slow isocontour) at and below 100 km depth. The depth axis is reversed as if the mantle structure was turned inside out (light pink is deep, red is shallower). Yellow bars show the anisotropy 50 km below the LAB, where asthenospheric anomalies tend to peak. Dashed blue lines indicate the cross-sections presented in Fig. 4.

a high lateral resolution of ~50 km, but little vertical resolution (Fig. 1a). Fast S-velocity directions strike roughly east–west under Rodrigues corridor, consistent across OBS and with earlier measurements on Réunion, Mauritius and Rodrigues island stations[26] (Fig. 1a). Along a central axis that connects Mauritius, Rodrigues and the CIR, fast directions strike almost exactly east–west. North of this axis, they have a south-pointing component (N100°E), whereas south of it, the anisotropy points slightly north (N80°E). West of Réunion, fast directions wrap around the leading edge of the hotspot track. Jointly these splitting observations suggest a latitudinal gathering of eastward flow, from relatively diffuse in the Mascarene Basin into a focused stream towards the spreading ridge, at least as wide as the instrumented area (~400 km latitudinally (Fig. 1a)). SKS phases[19] are split by 1–2 s (Fig. 1a), of which 80% probably originate in the asthenosphere (as indicated by forward propagation through the tomography model (Methods and Supplementary Fig. 7)). These substantial splits imply a 100–150 km thick flowing layer, assuming a typical intrinsic anisotropy of 3–5% in the flowing mantle[25].

Rayleigh-wave tomography yields azimuthal anisotropy as a function of depth, and extends beyond the instrumented areas to the basin scale, but with a lower lateral resolution of ~300 km (Supplementary Figs. 2, 3 and 5). Tomographically estimated anisotropy is superimposed on depth sections of isotropic $\delta V_s/V_s$ in Figs. 1 and 2, and on a 3D rendering of the MBAR in Fig. 3b. Within the MBAR (Figs. 2d–f and 3b), anisotropy is strong and aligns E–W to NW–SE, joining up well with SKS splits under the northern Rodrigues corridor (Fig. 1a). Anisotropy appears weak and incoherent under the corridor itself (Fig. 2d, 1f), seemingly in contradiction with splitting observations but explained if the (less resolving) surface waves averaged over different structures within and south of Rodrigues corridor.

Stark anisotropy contrasts between the MBAR asthenosphere and overlying lithosphere are evident in Figs. 2b versus 2d or 3a versus 3b, but this is best appreciated in east–west cross-sections

shown in Fig. 4, where the bars that indicate fast directions are arranged in vertical columns to highlight the changes of azimuthal anisotropy with depth. Under the Mascarene Basin and Réunion (red star in Fig. 4), the lithosphere anisotropy strikes roughly north–south (near-vertical bars), almost perpendicular to asthenospheric anisotropy. The transition in depth is marked by anisotropy minima. Almost everywhere these 'zero crossings' of anisotropy coincide with the isotropically imaged LAB (the sharp vertical transition from blue to red shades), a finding that lends credence to these anisotropy minima as alternative LAB markers. The observed LAB transition spans around 20 km vertically, a sharpness well resolved according to resolution tests (Methods and Supplementary Fig. 5).

Within the isotropically defined asthenosphere (red areas in Fig. 4), fast V_s azimuths tend to arrange into spindle-shaped vertical profiles, most clearly expressed in sections 18.5°S and 12.5°S. The anisotropy magnitude peaks in the middle of the slow layer and crosses zero at both its top and bottom. As the upper minimum marks the LAB, the lower seems to define the elusive asthenosphere–mesosphere boundary, which is poorly defined by isotropic $\delta V_s/V_s$. It is observed between 150 and 200 km depth across Fig. 4, bounding 100–150 km thick asthenosphere from below.

The occurrence of spindle-shaped anisotropy profiles is limited to areas of very slow isotropic V_s, that is, to the asthenosphere of the MBAR and Rodrigues corridor. South of the corridor (21.5°S and 26.5°S), spindles are weakly developed or absent, even though moderately slow $\delta V_s/V_s$ still delineates the asthenosphere isotropically.

The spindle-shaped anisotropy profiles resemble parabolic velocity profiles of a planar Poiseuille-type flow of fluid between two horizontal confining 'plates' (lithosphere and mesosphere). Poiseuille flow is actively driven by a horizontal pressure gradient[27,28], as would be caused by plume upwelling in the west. Assuming that the anisotropy is caused by strain and hence proportional to the vertical derivative of (horizontal) fluid flow, the parabola-shaped depth profile of Poiseuille flow in an isoviscous fluid should generate an anisotropy
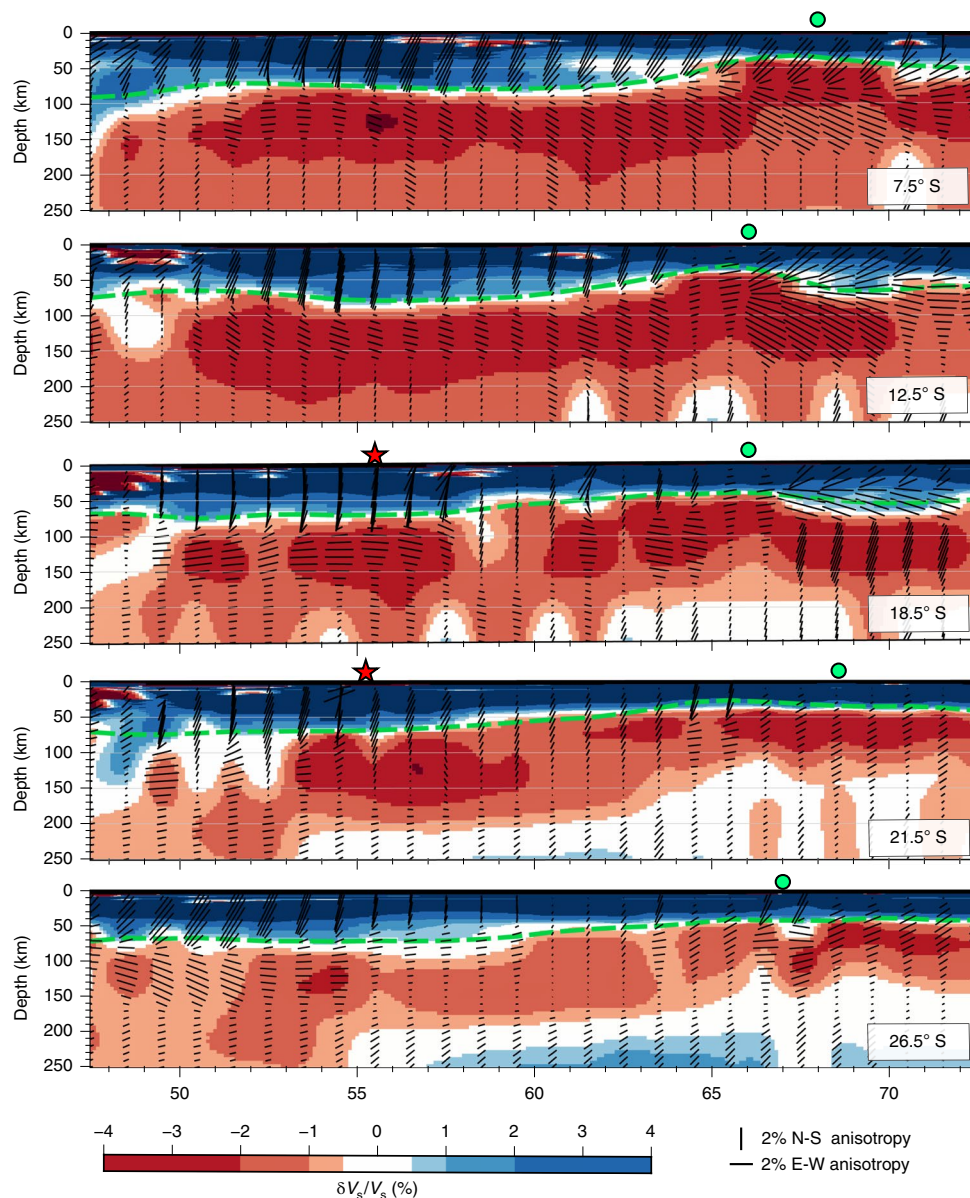
Fig. 4 | Upper mantle structure and Poiseuille-like asthenospheric flow beneath the Western Indian Ocean. East–west cross-sections through the MBAR (7.5° S, 12.5° S), Rodrigues corridor (18.5° S) and south (21.5° S, 26.5° S) of these two bodies of a very slow asthenosphere. Isotropic $\delta V_s/V_s$ is represented by the same colour scale as in Figs. 1 and 2. Azimuthal anisotropy is shown by black bars, in 10 km vertical increments. Horizontal and vertical bars indicate east–west and north–south striking directions, respectively. The anisotropy magnitude is normalized relative to the horizontal and vertical scale bars in the legend. Green circles and red stars mark the longitudes of the CIR and Réunion island, respectively. Green dashed lines indicate the 1,200 °C isotherm LAB estimates[21] shown in Fig. 3a.

minimum in the middle of the flow[28,29] (Supplementary Fig. 4), contrary to the actually observed maximum. Real mantle rheologies are, however, non-linear and temperature dependent. Hence, a viscosity minimum in the middle of the MBAR asthenosphere—compatible with the peak isotropic $\delta V_s/V_s$ observed there—would concentrate flow and hence anisotropy in the middle of the layer, as observed in Fig. 4 and schematized in Fig. 5 and Supplementary Fig. 4.

Alternatively, asthenosphere might be passively dragged by the overlying lithosphere, predicting completely different anisotropy profiles (Couette flow (Supplementary Fig. 4)). Intuition and geodynamic modelling[30,31] indicate that such an asthenospheric flow and anisotropy should be aligned with the (northeastward) motion of the overlying Somali and Indian Plates[32,33] (Supplementary Fig. 7), a stark mismatch to the MBAR's robustly observed west–east to

northwest–southeast striking anisotropy. Fluid velocities and anisotropy in Couette flow would peak at the LAB and taper downward[27] (Supplementary Fig. 4), as would anisotropy. Our resolution tests (Methods and Supplementary Fig. 5) indicate that such an anisotropy maximum at the LAB can be ruled out and that the observed minimum at the LAB is resolved. Hence, our observations robustly support the dominance of actively driven asthenospheric flow, directed (south)eastward towards the CIR (a sink of asthenosphere) and driven by a westerly source (a plume?).

Plume–ridge interaction beneath the CIR

In the lithosphere, fast azimuthal anisotropy is oriented north–south in the Cretaceous-aged Mascarene Basin and northeast–southwest in seafloor produced by the younger CIR (Fig. 3a), that is,
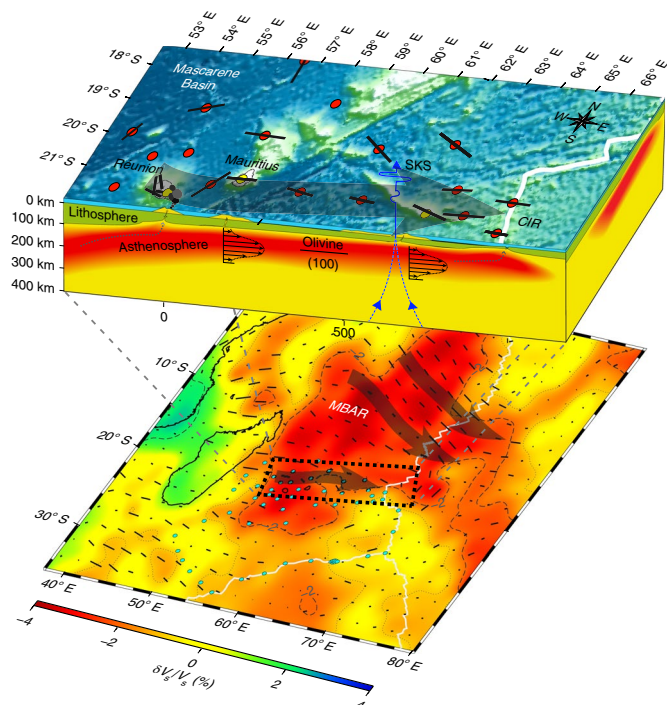
Fig. 5 | Conceptual summary of shallow and deep flows in the asthenosphere beneath the western Indian Ocean. The block diagram (roughly to scale) shows the shallow asthenospheric channel under the Rodrigues corridor, from Réunion towards the CIR, and its eastward Poiseuille-type flow velocity profile that aligns the olivine [100] fast axes east–west. Red dots are OBS locations and black bars are SKS splitting measurements. The lower map shows isotropic and anisotropic shear velocities at 140 km depth, and the dotted black rectangle indicates the extent of the block diagram. Grey interpretive arrows highlight the shallow, hotspot-to-CIR flow in the Rodrigues corridor asthenosphere, and the deeper, broader flows within the MBAR asthenosphere, towards and beyond the CIR. The horizontal scale at the base of the block diagram is in km.

consistently parallel to (palaeo)spreading directions as expected. Where MBAR asthenosphere spills under the CIR at latitudes ~6–17° S, a shallow layer of northeast–southwest anisotropy (parallel to the current CIR spreading) is underlain by a layer of northwest–southeast anisotropy (Fig. 4, clearest at 7.5° S below the green circle, and also at 12.5° S). Unlike everywhere else, this change of anisotropy direction beneath the spreading ridge occurs within the asthenosphere, not at the (isotropic) LAB. Hence, the superficial part of the MBAR appears to feed the accreting CIR, realigning its flow with the spreading, but the CIR's suction appears too weak to significantly drain or divert the MBAR's deeper, northwest–southeast directed flow. This flow extends to the Indo-Australian Plate, where additional large areas of slow asthenosphere are imaged (Figs. 2d–f, 3b and 4).

This hypothesis predicts that CIR basalts should sample the hotspot-influenced geochemistries of Rodrigues and MBAR flows. Indeed, basalts dredged in the Rodrigues CIR segment (17–21° S) require mixing between standard mid-ocean ridge basalt (MORB) and Réunion's ocean island basalt (OIB) signatures[12,13,15,34]. He³/He⁴ ratios are also intermediate between MORB and the Réunion OIB[14]. Between 8 and 12° S, where MBAR passes beneath the CIR, basalts are enriched, but geochemically distinct from the Rodrigues corridor samples[34]. Originally interpreted as a mantle upwelling other than Réunion, but also located ~1,000 km west of the CIR[34], our observations clarify that this second enriched reservoir is the MBAR.

Under the Rodrigues corridor, all the subsurface observations support Morgan's hypothesis of hotspot–ridge interaction[8], as summarized in Fig. 5. The Réunion hotspot supplies hot asthenosphere, which generates a horizontal pressure gradient and Poiseuille-type flow towards the asthenosphere-consuming CIR. This flow is focused by an east–west striking groove of thinned lithosphere, which facilitates the leakage of lavas to the surface and thus explains the presence of the Rodrigues Ridge's thickened crust and geochemical OIB signature. Groove-like thinning is implicit in Morgan's hypothesis, who reconstructed the Rodrigues corridor as the persistent line of flow from hotspot to eastward-drifting CIR over time, an evolution that exposed (only) this corridor of lithosphere to prolonged excess heat. Approaching the CIR, the flow channel's hot contents account for the anomalously swelled CIR segment[8,10,35] and its hotspot-influenced geochemistry.

Other examples of 'Morgan-type'[8] hotspot–ridge interaction have been investigated from surface evidence, for example, for Galapagos/Darwin[8,36,37] and Kerguelen/Amsterdam[8,16,38], but our results resolve this relatively small-scale (<1,000 km) flow phenomenon in the oceanic subsurface.

Much larger, hidden flow of asthenosphere

Surprisingly, our MBAR observations suggest yet another flow type towards the mid-ocean ridge, which is deeper and much broader than the Rodrigues channel flow. The Rodrigues corridor marks the MBAR's southern limit (Fig. 3b), and the asthenosphere in both is expressed similarly in isotropic and anisotropic S velocities, but the lithospheric lid is thicker above the MBAR (Figs. 3 and 4). This may explain the MBAR's limited surface expressions, which consist of an enriched CIR MORB signature[34] and the Mascarene Basin's unexpectedly shallow bathymetry (~500 m residual)[39]. East of the CIR, the MBAR flow may also be expressed in plate motion changes of the Capricorn plate[39].

The combination of enriched CIR basalts, very slow shear velocities, and Poiseuille-type anisotropy profiles unaligned with current CIR spreading or plate motion (Supplementary Fig. 7) strongly suggest that the MBAR asthenosphere is fed from some kind of deep upwelling. This could be Réunion's remnant plume head and/or younger plume tail[40]. This origin would require effective northeastward dragging of the plume asthenosphere by the formerly fast-moving Indian Plate (Couette-like flow), unlike the plate–asthenosphere decoupling implied by the present-day Poiseuille flow. Today's fast-moving Pacific Plate is, indeed, known to have motion-parallel, basin-scale fast anisotropy directions[41] and a clear Couette flow component[27,28].

A more intuitive source for the MBAR is a separate plume that rises beneath the Mascarene Basin. This would explain southeastward anisotropy towards the CIR and enriched MORB compositions at 8–12° S that are distinct from Réunion and Rodrigues[34]. However, our ongoing body-wave tomography work[42] indicates no deep upwelling north of Réunion, which leaves the possibility of a separate palaeo-upwelling under the Mascarene Basin that has since lost its connection to the deep mantle[40].

Below 100 km depth, the vast MBAR connects seamlessly to equally vast areas of slow $\delta V_s/V_s$ and a pronounced east–west anisotropy under the Indo-Australian Plate (Fig. 3b), which resembles asthenospheric fingering[43], as imaged by surface-wave tomography beneath the Pacific[44,45] and South Atlantic[46] oceans, other hotspot-rich regions. If all this asthenosphere is, indeed, sourced from deep mantle upwelling, the observed continuity of strong anisotropy (that is, flow) across large tracts of Indian Ocean points in the direction of a plume-fed asthenosphere[47,48]. This implies that the heat brought towards the surface by mantle plumes may remain largely trapped and overlooked beneath the oceans, with little or unexpected surface manifestations[39]. Owing to its vast spatial spread, MBAR-like asthenosphere tends to be perceived as the default state of a seismically

defined low-velocity asthenosphere in a sparsely instrumented ocean, rather than recognized as a large heat buffer fed by a localized deep mantle source. Much of this heat would be lost slowly and imperceptibly through conductive half-space cooling of the lithosphere overhead and mesosphere below, rather than through hotspot volcanism or mid-ocean ridge accretion. Hence, the recognition of the deep Mascarene Basin asthenosphere as plume sourced, as argued here from high-resolution seismological observations on the seafloor, calls for an upward revision of the plumes' relative contribution to the Earth's heat budget.

Online content

Any methods, additional references, Nature Research reporting summaries, source data, extended data, supplementary information, acknowledgements, peer review information; details of author contributions and competing interests; and statements of data and code availability are available at https://doi.org/10.1038/s41561-019-0479-3.

References

1. Morgan, W. J. Convection plumes in the lower mantle. *Nature* **230**, 42–43 (1971).
2. Courtillot, V., Davaille, A., Besse, J. & Stock, J. Three distinct types of hotspots in the Earth's mantle. *Earth Planet. Sci. Lett.* **205**, 295–308 (2003).
3. Courtillot, V. et al. Deccan flood basalts and the Cretaceous/Tertiary boundary. *Nature* **333**, 843–846 (1988).
4. Duncan, R. A. & Hargraves, R. B. $^{40}Ar/^{39}Ar$ geochronology of basement rocks from the Mascarene plateau, the Chagos bank and the Maldives ridge. *Proc. Ocean Drill. Program, Sci. Results* **115**, 43–51 (1990).
5. Montelli, R., Nolet, G., Dahlen, F. A. & Masters, G. A catalogue of deep mantle plumes: new results from finite-frequency tomography. *Geochem. Geophys. Geosyst.* **7**, Q11007 (2006).
6. French, S. W. & Romanovicz, B. Broad plumes rooted at the base of the Earth's mantle beneath major hotspots. *Nature* **525**, 95–101 (2015).
7. Ritsema, J. Evidence for shear velocity anisotropy in the lowermost mantle beneath the Indian Ocean. *Geophys. Res. Lett.* **27**, 1041–1044 (2000).
8. Morgan, W. J. Rodriguez, Darwin, Amsterdam, …, a second type of hotspot island. *J. Geophys. Res.* **83**, 5355–5360 (1978).
9. Duncan, R. A. The volcanic record of the Réunion hotspot. *Proc. Ocean Drill. Program, Sci. Results* **115**, 3–10 (1990).
10. Dyment, J., Lin, J. & Baker, E. T. Ridge–hotspot interactions: what mid-ocean ridges tell us about deep Earth processes. *Oceanography* **20**, 102–115 (2007).
11. McDougall, I., Upton, B. G. J. & Wadsworth, W. J. A geological reconnaissance of Rodriguez Island Indian Ocean. *Nature* **206**, 26–27 (1965).
12. Mahoney, J. J. et al. Isotopic and geochemical provinces of the western Indian Ocean spreading centers. *J. Geophys. Res.* **94**, 4033–4052 (1989).
13. Nauret, F. et al. Correlated trace element-Pb isotope enrichments in Indian MORB along 18–20° circle S, Central Indian Ridge. *Earth Planet. Sci. Lett.* **245**, 137–152 (2006).
14. Füri, E. et al. Helium isotope variations between Réunion Island and the Central Indian Ridge (17°–21°S): new evidence for ridge-hot spot interaction. *J. Geophys. Res.* **116**, B02207 (2011).
15. Murton, B. J., Tindle, A. G., Milton, J. A. & Sauter, D. Heterogeneity in southern Central Indian Ridge MORB: implications for ridge–hot spot interaction. *Geochem. Geophys. Geosyst.* **6**, Q03E20 (2005).
16. Okal, E. A. & Stewart, L. M. Slow earthquakes along oceanic fracture zones: evidence for asthenospheric flow away from hotspots? *Earth Planet. Sci. Lett.* **57**, 75–87 (1982).
17. Barruol, G. & Sigloch, K. Investigating La Réunion hot spot from crust to core. *EOS Trans. Am. Geophys. Union* **94**, 205–207 (2013).
18. Mazzullo, A. et al. Anisotropic tomography around La Réunion island from Rayleigh waves. *J. Geophys. Res.* **122**, 9132–9148 (2017).
19. Scholz, J.-R. et al. SKS splitting in the Western Indian Ocean from land and seafloor seismometers: plume, plate and ridge signatures. *Earth Planet. Sci. Lett.* **498**, 169–184 (2018).
20. Seton, M. et al. Global continental and ocean basin reconstructions since 200 Ma. *Earth-Sci. Rev.* **113**, 212–270 (2012).
21. Stixrude, L. & Lithgow-Bertelloni, C. Mineralogy and elasticity of the oceanic upper mantle: origin of the low-velocity zone. *J. Geophys. Res.* **110**, B03204 (2005).
22. Debayle, E. & Lévêque, J. J. Upper mantle heterogeneities in the Indian Ocean from waveform inversion. *Geophys. Res. Lett.* **24**, 245–248 (1997).
23. Ma, Z. & Dalton, C. A. Evolution of the lithosphere in the Indian Ocean from combined earthquake and ambient noise tomography. *J. Geophys. Res.* **122**, 354–371 (2017).
24. Nicolas, A. & Christensen, N. I. in *Composition, Structure and Dynamics of the Lithosphere–Asthenosphere System* Vol. 16 (eds Fuchs, K. & Froidevaux, C.) 111–123 (American Geophysical Union, 1987).
25. Mainprice, D., Barruol, G. & Ben Ismail, W. in *Earth's Deep Interior: Mineral Physics and Tomography from the Atomic to the Global Scale* Vol. 117 (eds Karato, S. I. et al.) 237–264 (American Geophysical Union, 2000).
26. Barruol, G. & Fontaine, F. R. Mantle flow beneath La Réunion hotspot track from SKS splitting. *Earth Planet. Sci. Lett.* **362**, 108–121 (2013).
27. Stotz, I. L., Iaffaldano, G. & Davies, D. R. Pressure-driven Poiseuille flow: a major component of the torque-balance governing Pacific Plate motion. *Geophys. Res. Lett.* **45**, 117–125 (2018).
28. Natarov, S. I. & Conrad, C. P. The role of Poiseuille flow in creating depth-variation of asthenospheric shear. *Geophys. J. Int.* **190**, 1297–1310 (2012).
29. Lin, P.-Y. P. et al. High-resolution seismic constraints on flow dynamics in the oceanic asthenosphere. *Nature* **535**, 538–541 (2016).
30. Becker, T. W. & Faccenna, C. Mantle conveyor beneath the Tethyan collisional belt. *Earth Planet. Sci. Lett.* **310**, 453–461 (2011).
31. Forte, A. et al. Joint seismic–geodynamic–mineral physical modelling of African geodynamics: a reconciliation of deep-mantle convection with surface geophysical constraints. *Earth Planet. Sci. Lett.* **295**, 329–341 (2010).
32. Morgan, W. J. & Morgan, J. P. in *Plates, Plumes, and Planetary Processes* (eds Foulger, G. R. & Jurdy, D. M.) 65–78 (Geological Society of America, 2007).
33. Argus, D. F., Gordon, R. G. & DeMets, C. Geologically current motion of 56 plates relative to the no-net-rotation reference frame. *Geochem. Geophys. Geosyst.* **12**, Q11001 (2011).
34. Kim, J., Pak, S.-J., Moon, J.-W., Lee, S.-M. & Stuart, F. M. Mantle heterogeneity in the source region of mid-ocean ridge basalts along the northern Central Indian Ridge (8°S–17°S). *Geochem. Geophys. Geosyst.* **18**, 1419–1434 (2017).
35. Hable, S., Sigloch, K., Stutzmann, E., Kiselev, S. & Barruol, G. Tomography of crust and lithosphere in the western Indian Ocean from noise cross-correlations of land and ocean bottom seismometers. *Geophys. J. Int.* **219**, 924–944 (2019).
36. Ito, G., Lin, J. & Gable, C. W. Interaction of mantle plumes and migrating mid-ocean ridges: implications for the Galapagos plume-ridge system. *J. Geophys. Res.* **102**, 15403–15417 (1997).
37. Mittal, T. & Richards, M. A. Plume–ridge interaction via melt channelization at Galápagos and other near-ridge hotspot provinces. *Geochem. Geophys. Geosyst.* **18**, 1711–1738 (2017).
38. Maia, M. et al. Building of the Amsterdam-Saint Paul plateau: a 10 Myr history of a ridge–hot spot interaction and variations in the strength of the hot spot source. *J. Geophys. Res.* **116**, B09104 (2011).
39. Iaffaldano, G., Davies, D. R. & DeMets, C. Indian Ocean floor deformation induced by the Réunion plume rather than the Tibetan Plateau. *Nat. Geosci.* **11**, 362–366 (2018).
40. Kumagai, I., Davaille, A., Kurita, K. & Stutzmann, E. Mantle plumes: thin, fat, successful, or failing? Constraints to explain hot spot volcanism through time and space. *Geophys. Res. Lett.* **35**, L16301 (2008).
41. Debayle, E. & Ricard, Y. Seismic observations of large-scale deformation at the bottom of fast-moving plates. *Earth Planet. Sci. Lett.* **376**, 165–177 (2013).
42. Tsekhmistrenko, M., Sigloch, K. & Hosseini, K. *Whole-Mantle Structure under the Réunion Hotspot in the Western Indian Ocean from Multifrequency P-wave Tomography* EGU2018-1076 (European Geosciences Union, 2018).
43. Sleep, N. H. Channeling at the base of the lithosphere during the lateral flow of plume material beneath flow line hot spots. *Geochem. Geophys. Geosyst.* **9**, Q08005 (2008).
44. French, S., Lekic, V. & Romanovicz, B. Waveform tomography reveals channeled flow at the base of the oceanic asthenosphere. *Science* **342**, 227–230 (2013).
45. Montagner, J. P. Upper mantle low anisotropy channels below the Pacific plate. *Earth Planet. Sci. Lett.* **202**, 263–274 (2002).
46. O'Connor, J., Jokat, W., Wijbrans, J. & Colli, L. Hotspot tracks in the South Atlantic located above bands of fast flowing asthenosphere driven by waning pulsations from the African LLSVP. *Gondwana Res.* **53**, 197–208 (2018).
47. Yamamoto, M., Morgan, J. P. & Morgan, W. J. in *Plates, Plumes, and Planetary Processes* (eds Foulger, G. R. & Jurdy, D. M.) 189–208 (Geological Society of America, 2007).
48. Morgan, J. P., Morgan, W. J., Zhang, Y. S. & Smith, W. H. F. Observational hints for a plume-fed, suboceanic asthenosphere and its role in mantle convection. *J. Geophys. Res.* **100**, 12753–12767 (1995).
49. Fontaine, F. R. et al. Crustal and uppermost mantle structure variation beneath La Réunion hotspot track. *Geophys. J. Int.* **203**, 107–126 (2015).

Methods

Seismological networks. The RHUM-RUM experiment[17] deployed 57 OBS (shown as triangles in Supplementary Fig. 1) in October 2012 with the French research vessel *Marion Dufresne* (cruise MD192[50]), and recovered them in December 2013 with the German *Meteor* (cruise M101[51]). Over half of the OBS were deployed over the 'Rodrigues corridor', stretching from Réunion to the CIR via Mauritius and Rodrigues (Fig. 2a and Supplementary Fig. 1).

The OBS measured continuous ground motion (velocity) along one vertical and two horizontal components. The network consisted of 9 stations equipped with Nanometrics Trillium 240 s broadband sensors (red triangles in Supplementary Fig. 1), loaned from the French INSU-IPGP pool (Institut National des Sciences de l'Univers–Institut de Physique du Globe de Paris), and 48 stations equipped with Guralp 60 s or 120 s wideband sensors (yellow triangles in Supplementary Fig. 1) from the German DEPAS pool (Deutsche Geräte-Pool für amphibische Seismologie) managed by the Alfred Wegener Institut. Technical details on the experiment and data preprocessing are published elsewhere[52–54].

RHUM-RUM also deployed 20 terrestrial stations on Réunion (10), the Îles Éparses and Mayotte in the Mozambique Channel (5) and South-East Madagascar (5) (white diamonds in Supplementary Fig. 1). For our SKS studies we further used the permanent island station MRIV on Mauritius (operated by the Mauritius Meteorological Services) and the stations RER (on Réunion) and RODM (on Rodrigues), operated by the GEOSCOPE network (https://doi.org/10.18715/GEOSCOPE.G). Also, 33 stations from the MACOMO experiment[55,56], installed between 2011 and 2013 in Madagascar (Supplementary Fig. 1), were integrated in the surface-wave tomography analysis[18].

Surface-wave tomography. For our Rayleigh-wave tomography[18] we used ~300 regional and teleseismic earthquakes with high signal-to-noise ratios recorded at ocean-bottom, island and land stations across the western Indian Ocean that allowed us to invert 9,000 phase-velocity measurements of fundamental-mode Rayleigh waves (30–300 s period) for isotropic $\delta V_s / V_s$, which is primarily a proxy for mantle temperature, and for azimuthally anisotropic $\delta V_s / V_s$, a proxy for current or past mantle flow.

For each earthquake–station path, we measured the phase velocities of fundamental-mode Rayleigh waves in the period range 30–300 s using the 'roller-coaster' method[57], and group velocities in the period range 16–250 s using time-frequency analysis. A 3D model of shear-wave velocity in the upper mantle was obtained as follows. First, we inverted the path-averaged phase and group velocities to obtain regionalized velocity maps for each period separately. Second, we combined all the phase and group velocity maps that corresponded to different periods and inverted them at each grid point to obtain the local S-wave velocity as a function of depth using a transdimensional inversion scheme. Third, these local models were recombined to obtain the 3D S-wave velocity and azimuthal anisotropy model with a lateral resolution of 300 km down to depths of 350 km (ref. [18]). Radial anisotropy could not be constrained as it requires Love-wave measurements, which are difficult to obtain from the noisy horizontal components of OBS.

Synthetic tests of the surface-wave tomography model, lateral resolution. We present two inversions of synthetic data aimed at testing the reliability and lateral resolution of the velocity regionalization. Supplementary Fig. 2 presents a generic checkerboard test and Supplementary Fig. 3 tests the robustness of an asthenospheric channel present in the actual inversion. Additional tests are given in Mazzullo et al. (2017)[18]. Path density and azimuthal coverage of the tests are identical to those used in the inversion of the real data (Supplementary Fig. 1).

The checkerboard test input (here, for phase velocities, a period of 100 s) consists of 500 km wide, vertical parallelepipeds of alternating slow and fast velocities (Supplementary Fig. 2a), which also include azimuthal anisotropy with fast directions that trend perpendicular from one block to the next (Supplementary Fig. 2c). Recovery is good for both isotropic (Supplementary Fig. 2b) and anisotropic (Supplementary Fig. 2d) structures, especially in the western Indian Ocean centred on the Réunion–Rodrigues and MBAR areas.

In Supplementary Fig. 3a, the resolution test input (here, for phase velocities, a period of 80 s) consists of a negative velocity anomaly modelled on a low-velocity channel under the Rodrigues corridor between Réunion island and the CIR. We considered a 1,000 km long and 200 km wide parallelepiped with an (isotropic) velocity anomaly of $\delta V_s / V_s = -3\%$ relative to the reference model (Supplementary Fig. 3a). Recovery of the overall structure is good (Supplementary Fig. 3b), with very little smearing in the north–south direction (the narrower dimension), and moderate smearing of ~200 km in the east–west direction.

Synthetic tests of the surface-wave tomography model, vertical resolution of azimuthal anisotropy. We performed inversions of synthetic data to check the vertical resolution of the surface-wave tomography model, specifically its ability to constrain azimuthal anisotropy as a function of depth. Anisotropy is caused by a differential movement in the rock matrix (shear strain). In the case of horizontal flow, the strain is due to differing horizontal flow velocities as a function of depth within the flowing layer (asthenosphere), that is, strain is a function of $\delta V_h / \delta z$, where V_h is horizontal fluid velocity and z is the depth below the

LAB. Supplementary Fig. 4 schematically compares the vertical profiles of fluid flow, shear and anisotropy in the asthenosphere for the cases of Couette and Poiseuille flows.

In the Couette flow case (Supplementary Fig. 4a), asthenosphere is dragged by the overlying lithosphere. Strain and azimuthal anisotropy are expected to peak at the LAB (where V_h decreases most rapidly with depth) and to decrease with depth, a pattern suggested by numerical models[58]. In the case of Poiseuille flow (Supplementary Fig. 4b,c), the lithosphere and asthenosphere are decoupled and horizontal flow is driven by a horizontal pressure gradient (which is constant as a function of depth). In an isoviscous asthenosphere (Supplementary Fig. 4b), one expects a parabolic flow pattern as a function of depth, which results in a minimum shear and anisotropy in the middle of the asthenosphere[28,29] and local maxima on either side of the minimum, leading to a 'two-spindle' anisotropy profile unlike the 'one-spindle' profile we actually observed in the MBAR asthenosphere. In the non-linear, strongly temperature-dependent rheology of mantle rocks, the asthenosphere is likely to have internal viscosity variations and to be softest in the middle, where isotropic $\delta V_s / V_s$ (a proxy for temperature and/or water content) is observed to peak. The resulting Poiseuille flow (Supplementary Fig. 4c) concentrates shear in the weakest zone and predicts the one-spindle anisotropy profile observed in the MBAR.

Our resolution tests presented in Supplementary Fig. 5 are aimed at testing whether the one-spindle profile of Supplementary Fig. 4c is resolvable given our tomographic data coverage, and whether the dominance of plate drag (the Couette profile of Supplementary Fig. 4a) can be ruled out.

In both the Couette and Poiseuille cases, we considered a homogeneous, 80 km thick lithosphere above a 120 km thick flowing asthenosphere (depth 80–200 km), underlain by a mesosphere half-space, which does not move nor deform. The lithosphere features a 2% anisotropy with a fast direction of N030°E, which is modelled on the 'frozen in' anisotropy observed for the Mascarene Basin lithosphere (Figs. 2b, 3a and 4) and conforms to the palaeo-spreading direction.

For the Couette flow test, the dragging Somali lithosphere is modelled to move N075°E (Supplementary Fig. 5a), which induces an asthenospheric anisotropy of the same strike (N075°E) at an angle of 45° from the lithospheric anisotropy (Supplementary Fig. 5b, red line). Asthenospheric anisotropy is considered to reach its peak of 3% at the LAB, and gradually decrease to 0% at a 200 km depth (Supplementary Fig. 5c, red line).

In the case of (non-isoviscous) Poiseuille flow (Supplementary Figs 4c and 5d), lithospheric motion has no influence on the asthenospheric anisotropy as the two layers are decoupled. We modelled the asthenospheric anisotropy to strike N060°W (Supplementary Fig. 5e, red line), as observed for the asthenosphere of the MBAR, with a maximum amplitude of 3% in the middle of the layer (125 km depth) and zero amplitude at its top and bottom (Supplementary Fig. 5f, red line).

The S-wave velocity was parametrized[59] as:

$$V_s = \sqrt{\frac{(L + G_c \cos 2\psi + G_s \sin 2\psi)}{\rho}}$$

where L, G_c and G_s are anisotropy parameters defined from combinations of the elastic coefficients: $L = 1/2(C_{44} + C_{55})$, $G_c = 1/2(C_{55} - C_{44})$ and $G_s = C_{54}$ (see ref. [59] for explicit definitions of these parameters); and ρ is density. The anisotropy parameters inverted are L, G_c and G_s as a function of depth. The percentage of anisotropy is $A = 100\% \frac{\sqrt{(G_c^2 + G_s^2)}}{L}$ and the anisotropy azimuth is $\psi = \operatorname{atan}\left(\frac{G_s}{G_c}\right)$. For details on the inversion scheme, see section (4) in Mazzullo et al.[18].

The resolution test results are plotted as blue dotted lines in Supplementary Fig. 5b,c,e,f. Although imperfect data coverage and wave sensitivities have a smoothing effect on the recovered vertical profiles, the azimuths and amplitudes of anisotropy are retrieved in both models. The magnitude of anisotropy appears to be a robust discriminating factor between the two competing models.

In the Couette flow case, the test faithfully recovers the high amplitude of anisotropy at the LAB (Supplementary Fig. 5c, blue), a result that is clearly distinguishable from the zero crossings observed for the MBAR and recovered to good approximation by the Poiseuille-case test (see below). Regarding directions, the input of a 45° jump of anisotropy azimuth across the LAB in Supplementary Fig. 5b is recovered as a gradual rotation from lithospheric to asthenospheric strike over a depth range from ~30 km above the LAB to ~30 km below it.

In the Poiseuille flow case, the test robustly resolves a pronounced minimum of anisotropy amplitude at the LAB, almost matching the input of zero (Supplementary Fig. 5f, blue versus red). This result is robustly distinguishable from the Couette flow test (Supplementary Fig. 5c, blue) and is consistent with our MBAR observations. The spindle-shaped input pattern for the asthenosphere is well recovered. The jump of anisotropy azimuths across the LAB (Supplementary Fig. 5e, red) is smoothed over a smaller vertical range (Supplementary Fig. 5e, blue) than in the Couette test (Supplementary Fig. 5b, blue), consistent with that observed.

The Couette flow scenario makes a clear prediction for the asthenospheric direction of anisotropy (northeastward), and this prediction is clearly distinct from the observed MBAR direction (southeastward). As the anisotropy directions are well recovered by the tests, our observations provide strong evidence against a dominance of Couette flow.

The tests suggest that the observed absence (or 'zero-crossing') of anisotropy at the LAB is a real feature, as are the spindle-shaped anisotropy profiles observed in the asthenosphere in Fig. 4. This supports the dominance of Poiseuille-like flow in the Mascarene Basin asthenosphere, which implies that lithosphere and asthenosphere are largely decoupled in this region.

Across the asthenosphere–mesosphere boundary, the azimuths are recovered very accurately, and if one had to pick the asthenosphere–mesosphere boundary from the vertical profile of anisotropy magnitude, the result would not differ much whether it was done on the test input or output curves. This supports our claim that the lower ends of the anisotropy spindles observed in Fig. 4 should be good estimates for the depth of the asthenosphere–mesosphere boundary, the lower limit of the flowing layer.

Tomography-based estimates of lithospheric thickness (LAB depth). We estimated the lithospheric thickness in the western Indian Ocean (blue shades in Fig. 3a) using two different approaches, both based on isotropic shear-wave velocities V_{s0} obtained from surface-wave tomography[18]:

1. LAB depth equals the depth at which the minimum (that is, the largest negative value) of the vertical gradient in V_{s0} is located[60] or, visually speaking, the most rapid vertical transition from blue to red on the tomographic colour scale of Supplementary Fig. 6.
2. LAB depth equals the depth of the 1,200 °C isotherm (or, alternatively, the 1,100 or 1,300 °C isotherm), which is determined by an empirical formula that relates isotropic shear-wave velocities to rock temperature according to Stixrude and Lithgow-Bertelloni[21].

To avoid unrealistic lateral jumps for either approach, we smoothed the resulting lithospheric thickness for each map point by averaging over its eight closest neighbours, that is, over a radius of ~150 km.

The LAB depth estimates obtained from these methods are compared in Supplementary Fig. 6 (green lines) on an east–west tomography cross-section located at 10.5° S. There is good agreement between the two methods, in particular, beneath the Mascarene Basin and the CIR, and hence we show only the 1,200 °C LAB estimate in the cross-sections of Fig. 4. The same 1,200 °C LAB estimates (laterally smoothed) are shown in the lithospheric thickness map of Fig. 3a. Our tomography-derived LAB depth values are independently confirmed beneath islands by, and in good agreement with, depths obtained from a joint inversion of receiver function and surface-wave dispersion data, which used permanent island stations[49]. They found LAB depths of ~70 km beneath Réunion, ~50 km beneath Mauritius and ~25 km beneath Rodrigues (circles filled with the appropriate blue shades in Fig. 3a). The consistency of these different LAB estimates suggests a rather strong temperature gradient and therefore a sharp lithosphere–asthenosphere transition, as also observed in the northwestern Pacific Ocean[61,62].

Empirically, we found that asthenospheric anisotropy and negative isotropic $\delta V_s / V_s$ both tend to peak ~50 km beneath the 1,200 °C LAB. For a representative summary of asthenospheric flow (Fig. 3b), we therefore extracted tomographic anisotropy values along an undulating hypersurface that runs 50 km beneath the 1,200 °C LAB (white dashed lines in Supplementary Fig. 6).

Reconciling tomography and shear-wave splitting results. Observations of the splitting of SKS waves have been used to scan continents[63–65] and more recently the oceans[66–68] for (upper mantle) seismic anisotropy, which is accepted to result from crystal-preferred orientations of the rock-forming minerals[24,25].

Prior to the RHUM-RUM experiment, SKS splitting measurements in the western Indian Ocean were limited to Madagascar[56,69] and the islands of Réunion[26,70,71], Mauritius, Seychelles[72] and Rodrigues[26]. To analyse the RHUM-RUM data[19], we used teleseismic earthquakes of $M_w \geq 5.8$ at epicentral distances that ranged from 85 to 130° and measured the fast polarization axis (ϕ) and splitting delay time (δt) using the SplitLab software[73]. Measurements were performed using the eigenvalue approach[63], after carefully correcting for horizontal sensor orientations of the OBS[53].

Reconciling anisotropy observations from body and surface waves has been challenging for a long time[74–76] and is not a primary purpose of this article. The lateral resolution of SKS splitting measurements is ~50 km at a 100 km depth, whereas our surface-wave tomography provides a lateral resolution of ~300 km. An apparent observational contradiction that probably results from these different sensitivities concerns the Rodrigues corridor. SKS splits along the corridor (Fig. 1a) indicate strong east–west striking fast directions, whereas surface-wave anisotropy is relatively weak and diffuse in this region (Figs. 2d and 3b). SKS results are expected to be robust because individual measurements are independent (the station spacing is larger than the measurement sensitivity zone of ~50 km) and consistently yield the same strong east–west directions. Moreover, tomography sees the same strong east–west anisotropy just slightly further north in the MBAR. At face value, the surface-wave anisotropy is at odds with the SKS splits, but taken together, this leaves the explanation that the anisotropy in the Rodrigues corridor is strong and consistently aligned east–west, just like in the MBAR further north, but that the relatively narrow corridor (~1,000 km × 400 km) is sharply bounded, especially to the south, by structure that is very different. This would destroy any MBAR-like clarity in the surface-wave result because its resolution length of ~300 km would average over structures inside and outside the corridor.

Predicting SKS splitting parameters from the anisotropic surface-wave model. The quantity and quality of our SKS measurements was not sufficient to separately infer the respective splitting contributions of the lithosphere and asthenosphere. Hence, we calculated theoretical SKS splitting parameters for these two layers from our surface-wave tomography model. Surface-wave tomography confidently constrains the vertical profiles of V_{s0} and anisotropic fast split directions, but its lateral resolution of ~200–300 km is low compared to that of the SKS measurements (~50 km). This means that SKS splits forward-predicted through a tomography model will differ from the actual SKS observations, to the extent that the Earth structure is heterogeneous on such length scales.

We use the Rayleigh-wave model's n anisotropic depth layers[77] to forward-predict the fast split directions and delay times acquired beneath each seismic station for three simple cases: (1) only in the lithospheric layer (from 25 km depth to the LAB), (2) only in the asthenospheric layer (LAB to 300 km depth) and (3) in the combined lithosphere + asthenosphere package, that is, 25–300 km depth).

SKS splitting predictions for only the lithosphere (Supplementary Fig. 7a, orange bars) show clear north–south trending fast split directions throughout the area west of Réunion and Mauritius, with delay times <0.3 s (that is, small compared to the observations, black bars). The magnitude of anisotropy is less robustly estimated by tomography (typically underpredicted), which probably explains our persistent underprediction of SKS splits. We attribute the north–south trending fast split pattern to the identical palaeo-spreading direction of the Mascarene Basin[19,20], which formed this lithosphere between 60 and 80 Ma.

Between Mauritius and the CIR, the predicted lithospheric split times are even smaller, probably a combined effect of a thinner lithosphere[49] towards the CIR and a lower amplitude of the frozen-in anisotropy.

For the asthenosphere (Supplementary Fig. 7b), splitting predictions generally strike east–west, especially close to the CIR, and show a good directional agreement with observed fast splits from the SKS phases. At several stations between Réunion Island and Rodrigues Ridge, the predicted fast split directions trend northeast–southwest. We attribute this to the presence of slight singularities (undesired, non-smoothed artefacts) in the Rayleigh wave model at depths >200 km (for example, the middle panel in Fig. 4 at 60.5° E), which cause this rotation in the modelled directions. Importantly, between Réunion and the CIR, we predict asthenospheric delay times as high as 1 s, much higher than the predicted contribution of the overlying lithosphere (Supplementary Fig. 7a). Assuming the same ratio holds for the two layers' contributions to the actually observed SKS splits, this result implies that ~80% of the observed SKS split times stem from the asthenosphere, which justifies their interpretation in terms of east–west-directed asthenospheric flow. In a 100–150 km thick asthenosphere (Figs. 4 and 5), these splitting magnitudes would be produced vertically from a uniform 3–5% V_s anisotropy[25], or an accordingly stronger anisotropy in the central maximum of a spindle profile. This dominance of asthenospheric anisotropy is also visible in Supplementary Fig. 7c, where the combined lithosphere + asthenosphere predictions in the Rodrigues corridor look very similar to those in Supplementary Fig. 7b.

Data availability

The authors declare that data supporting the findings of this study are freely available from the RESIF data centre (http://seismology.resif.fr, https://doi.org/10.15778/RESIF.YV2011).

The RHUM-RUM dataset (https://www.fdsn.org/networks/detail/YV_2011/) has been assigned the FDSN network code YV and is hosted and freely accessible at the French RESIF data centre (http://seismology.resif.fr). MACOMO data are archived at the IRIS DMC (http://www.iris.edu) under the FDSN network code XV (https://doi.org/10.7914/SN/XV_2011). The individual RHUM-RUM SKS splitting measurements presented in this article can be found online in the SKS splitting data base https://doi.org/10.18715/sks_splitting_database and mirrored and accessible at IRIS (Incorporated Research Institutions for Seismology) at https://ds.iris.edu/spud/swsmeasurement. We acknowledge the GEOSCOPE network (https://doi.org/10.18715/GEOSCOPE.G) for installing and maintaining permanent stations in the Indian Ocean.

Code availability

The shear-wave splitting measurements were performed with the MATLAB-based SplitLab code available at https://github.com/IPGP/splitlab. The surface-wave tomography codes are not available online because they are tailored for laboratory work, but they can be requested by email to E.S. or S.K.

References

50. Barruol, G. *Marion Dufresne MD192 Cruise Report Sept–Oct 2012* https://doi.org/10.13140/2.1.2492.0640 (2013).
51. Sigloch, K. *Cruise Report R/V Meter, Cruise No. 101*: *Seismological Imaging of a Mantle Plume under La Réunion, Western Indian Ocean* https://doi.org/10.2312/cr_m101 (2014).
52. Stähler, S. C. et al. Performance report of the RHUM-RUM ocean bottom seismometer network around La Réunion, western Indian Ocean. *Adv. Geosci.* **41**, 43–63 (2016).

53. Scholz, J.-R. et al. Orienting ocean-bottom seismometers from P- and Rayleigh waves polarizations. *Geophys. J. Int.* **208**, 1277–1289 (2017).
54. Hable, S., Sigloch, K., Barruol, G., Stähler, S. C. & Hadziioannou, C. Clock errors in land and ocean bottom seismograms: high-accuracy estimates from multiple-component noise cross-correlations. *Geophys. J. Int.* **214**, 2014–2034 (2018).
55. Pratt, M. J. et al. Shear velocity structure of the crust and upper mantle of Madagascar derived from surface wave tomography. *Earth Planet. Sci. Lett.* **458**, 405–417 (2017).
56. Ramirez, C. et al. Complex seismic anisotropy in Madagascar revealed by shear wave splitting measurements. *Geophys. J. Int.* **215**, 1718–1727 (2018).
57. Beucler, E., Stutzmann, E. & Montagner, J. P. Surface wave higher-mode phase velocity measurements using a roller-coaster-type algorithm. *Geophys. J. Int.* **155**, 289–307 (2003).
58. Tommasi, A. Forward modeling of the development of seismic anisotropy in the upper mantle. *Earth Planet. Sci. Lett.* **160**, 1–13 (1998).
59. Montagner, J. P. & Nataf, H. C. A simple method for inverting the azimuthal anisotropy of surface-waves. *J. Geophys. Res.* **91**, 511–520 (1986).
60. Burgos, G. et al. Oceanic lithosphere–asthenosphere boundary from surface wave dispersion data. *J. Geophys. Res.* **119**, 1079–1093 (2014).
61. Kawakatsu, H. et al. Seismic evidence of sharp lithosphere–asthenosphere boundaries of oceanic plates. *Science* **324**, 499–502 (2009).
62. Kawakatsu, H. & Utada, H. Seismic and electrical signatures of the lithosphere–asthenosphere system of the normal oceanic mantle. *Ann. Rev. Earth Planet. Sci.* **45**, 139–167 (2017).
63. Silver, P. G. & Chan, W. W. Shear wave splitting and subcontinental mantle deformation. *J. Geophys. Res.* **96**, 16429–16454 (1991).
64. Silver, P. G. Seismic anisotropy beneath the continents: probing the depths of geology. *Ann. Rev. Earth Planet. Sci.* **24**, 385–432 (1996).
65. Vinnik, L. P., Farra, V. & Romanovicz, B. Azimuthal anisotropy in the earth from observations of SKS at geoscope and NARS broadband stations. *Bull. Seismol. Soc. Am.* **79**, 1542–1558 (1989).
66. Barruol, G. et al. Mapping upper mantle flow beneath French Polynesia from broadband ocean bottom seismic observations. *Geophys. Res. Lett.* **36**, L14301 (2009).
67. Martin-Short, R., Allen, R. M., Bastow, I. D., Totten, E. & Richards, M. A. Mantle flow geometry from ridge to trench beneath the Gorda–Juan de Fuca plate system. *Nat. Geosci.* **8**, 965–969 (2015).
68. Takeo, A. et al. Seismic azimuthal anisotropy in the oceanic lithosphere and asthenosphere from broadband surface wave analysis of OBS array records at 60 Ma seafloor. *J. Geophys. Res.* **121**, 1927–1947 (2016).
69. Reiss, M. C. et al. Seismic anisotropy of the lithosphere and asthenosphere beneath southern Madagascar from teleseismic shear wave splitting analysis and waveform modeling. *J. Geophys. Res.* **121**, 6627–6643 (2016).
70. Barruol, G. & Ben Ismail, W. Upper mantle anisotropy beneath the African IRIS and Geoscope stations. *Geophys. J. Int.* **146**, 549–561 (2001).
71. Behn, M. D., Conrad, C. P. & Silver, P. G. Detection of upper mantle flow associated with the African Superplume. *Earth Planet. Sci. Lett.* **224**, 259–274 (2004).
72. Hammond, J. O. S. et al. Upper mantle anisotropy beneath the Seychelles microcontinent. *J. Geophys. Res.* **110**, B11401 (2005).
73. Wuestefeld, A., Bokelmann, G. H. R., Zaroli, C. & Barruol, G. SplitLab: a shear-wave splitting environment in Matlab. *Computer Geosci.* **34**, 515–528 (2008).
74. Griot, D. A., Montagner, J. P. & Tapponnier, P. Confrontation of mantle seismic anisotropy with two extreme models of strain in Asia. *Geophys. Res. Lett.* **25**, 1447–1450 (1998).
75. Wuestefeld, A., Bokelmann, G. H. R., Barruol, G. & Montagner, J. P. Identifying global seismic anisotropy patterns by correlating shear-wave splitting and surface-wave data. *Phys. Earth Planet. Int.* **176**, 198–212 (2009).
76. Becker, T. W. & Lebedev, S. & Long, M. D. On the relationship between azimuthal anisotropy from shear waves splitting and tomographic models. *J. Geophys. Res.* **117**, B01306 (2012).
77. Silver, P. G. & Savage, M. K. The interpretation of shear-wave splitting parameters in the presence of two anisotropic layers. *Geophys. J. Int.* **119**, 949–963 (1994).

Author contributions
G.B., K.S., J.-R.S., A.M., E.S., S.K., F.R.F. and J.-P.M. performed the analysis of the data, G.B. and K.S. were in charge of data acquisition and pre-processing, and led the writing of the manuscript. All the authors participated in interpreting the results.

Competing interests
The authors declare no competing interests.

Additional information
Supplementary information is available for this paper at https://doi.org/10.1038/s41561-019-0479-3.

Correspondence and requests for materials should be addressed to G.B.

Peer review information Primary Handling Editor(s): Melissa Plail; Rebecca Neely.

Reprints and permissions information is available at www.nature.com/reprints.